ProLB: A lattice Boltzmann solver of large-eddy simulation for atmospheric boundary layer flows

Yongliang Feng[1], Johann Miranda[1], Shaolong Guo[1], Jérôme Jacob[1], Pierre Sagaut[1]

[1]Aix Marseille Univ, CNRS, Centrale Marseille, M2P2 UMR 7340, 13451 Marseille, France

Key Points:

- An efficient large-eddy simulation tool within framework of lattice Boltzmann method is developed for simulating the dynamics of atmospheric boundary layers and urban flows;
- Immersed Boundary approach coupled with wall models is introduced to handle flows in complex configurations, with application to turbulent flows in realistic urban areas;
- The basic core, wall models, subgrid models and interaction terms are described, implemented and assessed in various micro-meteorological flows and urban flows;

Corresponding author: Pierre Sagaut, pierre.sagaut@univ-amu.fr

Abstract

A large-eddy simulation (LES) tool is developed for simulating the dynamics of atmospheric boundary layers using lattice Boltzmann method (LBM), which is an alternative approach for computational fluid dynamics and proved to be very well suited for the simulation of low-Mach flows. The equations of motion are coupled with the global complex physical models considering the coupling among several mechanisms, namely basic hydrothermodynamics and body forces related to stratification, Coriolis force, canopy effects, humidity transport and condensation. Mass and momentum equations are recovered by an efficient streaming, collision and forcing process within the framework of LBM while the governing equations of temperature, liquid and vapor water fraction are solved using a finite volume method. The implementation of wall models for atmospheric boundary layer, subgrid models and interaction terms related to multiphysic phenomena (e.g. stratification, condensation) is described, implemented and assessed in this study. An Immersed Boundary approach is used to handle flows in complex configurations, with application to flows in realistic urban areas. Applications to both wind engineering and atmospheric pollutant dispersion are illustrated.

Plain Language Summary

We have described a new tool for LES of atmospheric flows in this paper. Large-eddy simulation (LES) with the lattice Boltzmann method (LBM) was used to simulate dry and cloudy atmospheric boundary layers (ABL), along with flows in complex urban areas. To validate our LBM-LES solver, we first simulated the four basic ABL cases coming from the previous intercomparison of LES codes. These were the neutral, convective, stable, and cloudy convective boundary layers. Then three extra cases for ABL with canopy effects were performed by our solver. The altitude-dependent drag force and heat release source term were introduced and assessed in the present solver compared reference data. At last, the ProLB tool was successfully assessed considering two urban flow configurations: wind prediction in Shinjuku district in Tokyo, and gaseous pollutant dispersion in the Champs Elysées district in Paris. In both cases, very satisfactory comparisons with experimental data were recovered.

———————————————–

1 Introduction

The atmospheric boundary layer (ABL) ranges from hundreds of meters to several kilometers depending on meteorological conditions, mainly wind, temperature and humidity. Thus, structure of ABL is modified by the daily cycle of heating and cooling over Earth's surface producing three canonical types of boundary layers: convective or unstable, neutral, and stable boundary layers. Convective boundary layer is commonly observed during day when the surface is heated by the sun resulting in a positive buoyancy force, while stable boundary layer occurs during night when surface is cooled by radiation producing a negative buoyancy force, and neutral boundary layer is the case between the former two with little or no buoyancy.

The structure of ABL has an important effect on anthropic activities such as mesoscale weather forecasting or pollutant dispersion in urban areas [*Fernando et al.*, 2001]. To better understand ABL and related urban processes, numerical simulation is a good complement to field measurements and wind tunnel experiments [*Blocken*, 2015]. In the past much attention has been paid to the accurate CFD modeling of the atmospheric boundary layer (ABL), both using Reynolds averaged Navier-Stokes (RANS) and Large-eddy Simulation (LES) approaches.

Large-eddy Simulation (LES) [*Sagaut*, 2006], which is a high-fidelity approach for the unsteady simulation of turbulent flows, has been successfully applied to simulation of ABL [e.g. *Andren et al.*, 1994; *Nieuwstadt et al.*, 1993; *Beare et al.*, 2006; *Siebesma et al.*, 2003]. Among the key issues raised in the development of LES, one must mention the development of i) subgrid models to account for the influence of unresolved scales of motion on the resolved ones, ii) wall models when the grid is too coarse to allow for the use of the no-slip boundary condition at solid walls and iii) well suited numerical schemes that ensure stable simulations without masking the physical subgrid model effects.

Most of numerical tools for simulation of atmospheric boundary layer flows are developed in the framework of conventional finite difference or finite volume methods, e.g, UCLA-LES [*Stevens et al.*, 2005], PALM [*Maronga et al.*, 2015], ICON [*Dipankar et al.*, 2015], MicroHH [*Heerwaarden et al.*, 2017], PyCLES [*Pressel et al.*, 2015], EULAG[*Prusa et al.*, 2008]. The lattice Boltzmann method (LBM) is an alternative approach to simulation of complex fluid dynamic problems, which is a recast the Navier-Stokes equations in a form of simplified kinetic equations for the time evolution of distribution

function of designer particles, with the basic rules of propagation on a regular space-filling lattice and collision at the lattice nodes. Thanks to its advantages for massively parallel computing as well as its high computational efficiency and low numerical dissipation for unsteady flows, the LB methods quickly extended to large scale and spread towards exascale applications: automatic shape optimization of full-scale vehicles [*Cheylan et al.*, 2019], urban scale environment flows [*Ahmad et al.*, 2017; *Jacob and Sagaut*, 2018], meteorological flows [*Feng et al.*, 2019a], and complex biological flows [*Chateau et al.*, 2017] have been successfully addressed, often with outstanding results.

Large-eddy simulation has been implemented within the lattice Boltzmann framework using mainly the eddy viscosity model [e.g. *Hou et al.*, 1994; *Eggels*, 1996; *Teixeira*, 1998; *Yu et al.*, 2006; *Premnath et al.*, 2009a,b; *Bartlett et al.*, 2013]. The main idea in this approach is that subgrid scale dynamics can be parameterized via a turbulent or eddy viscosity that is added to the molecular viscosity giving a total viscosity to be used in the LBM algorithm. Two approaches has been used to calculate the turbulent contribution. Several extensions have been proposed for compressible flows of low-speed thermal flows but, to the knowledge of the authors, a LBM-based LES approach for atmospheric flows including stratification/buoyancy effects, humidity, condensation effects and complex media such has forest canopy has not been proposed up to now.

This paper describes a lattice Boltzmann tool for large-eddy simulation of turbulent flows and thermal convection in atmospheric boundary layers, including neutral, stable, convective, and cloudy convective atmospheric boundary layers as well as urban flows. The paper is organized as follows. Section 2 reviews governing macroscopic equations along with condensation and subgrid model. Section 3 presents the lattice Boltzmann method, the finite difference method for water transport, and wall model implementation in boundary conditions. Section 4 investigates and discusses simulations on neutral, stable and convective ABL with canopy effects, as well as cumulus convection with phase change. The LBM-LES tool is then assessed considering two urban flow configurations in Sec. 5. Finally, Section 6 summarizes the capabilities and assessment of the present tool and draws perspectives.

2 Equations of motion

The atmosphere is assumed to be a mixture of dry air, water vapor, and liquid water, with respective mass fractions q_d, q_v and q_l (q_v being often referred to as specific humidity). A well-known approximation in the study of atmospheric and oceanic flows is the so-called Boussinesq approximation, which basically assumes that density variations due to buoyancy forces are small compared to a reference state. The reference state is taken to be a hydrostatic state (ρ_0, p_0, T_0). Commonly, hydrostatic pressure p_0 and T_0 decrease with height by

$$\frac{\mathrm{d}p_0}{\mathrm{d}z} = -\rho_0 g, \quad \frac{\mathrm{d}T_0}{\mathrm{d}z} = -\frac{g}{c_p} \tag{1}$$

Instead, one often uses the potential temperature θ

$$\theta = T\left(\frac{p_0(0)}{p_0(z)}\right)^{R_\mathrm{d}/c_\mathrm{p}} \tag{2}$$

Since $\mathrm{d}\theta_0 = 0$ in the isentropic reference state, one find that the reference potential temperature is constant, $\theta_0 = \Theta_0$.

2.1 Navier-Stokes equations

The governing equations of turbulent flows in atmospheric boundary layers are the filtered Navier-Stokes equations under the Boussinesq approximation.

$$\frac{\partial u_i}{\partial x_i} = 0 \tag{3a}$$

$$\frac{\partial u_i}{\partial t} + \frac{\partial u_j u_i}{\partial x_j} = -\frac{1}{\rho_0}\frac{\partial p''}{\partial x_i} + \frac{\partial}{\partial x_j}\left(\nu\frac{\partial u_i}{\partial x_j} - \overline{u_i' u_j'}\right) + F_{b,i} + F_{c,i} \tag{3b}$$

where u_i denotes the components of the velocity vector (u_x, u_y, u_z) and x_i represents the components of the position vector (x, y, z). The hydrodynamic pressure $p'' = p - p_0(z)$ represents the departure of the pressure p from reference state pressure $p_0(z)$. $F_{b,i}$ is the buoyancy term due to the gravity. $F_{c,i}$ is the Coriolis term due to the Earth's rotation. The turbulent stress $\overline{u_i' u_j'}$ denotes the subgrid momentum flux, which is responsible for the complicated chaotic nonlinear nature of turbulent flows.

2.2 Temperature and water

Associated prognostic conservation equations for the temperature liquid and vapor mass fractions are (the air mass fraction being deduced as $q_d = 1 - q_v - q_l$)

$$\frac{\partial \theta}{\partial t} + u_i \frac{\partial \theta}{\partial x_i} = \frac{\partial}{\partial x_i}\left(D_\theta \frac{\partial \theta}{\partial x_i} - \overline{\theta' u_i'} \right) + \frac{L_v \theta}{c_p T} \dot{Q} \tag{4a}$$

$$\frac{\partial q_v}{\partial t} + u_i \frac{\partial q_v}{\partial x_i} = \frac{\partial}{\partial x_i}\left(D_q \frac{\partial q_v}{\partial x_i} - \overline{q_v' u_i'} \right) - \dot{Q} \tag{4b}$$

$$\frac{\partial q_l}{\partial t} + u_i \frac{\partial q_l}{\partial x_i} = \frac{\partial}{\partial x_i}\left(D_q \frac{\partial q_l}{\partial x_i} - \overline{q_l' u_i'} \right) + \dot{Q} \tag{4c}$$

Here, c_p is the mass heat capacity of dry air; D_θ and D_q are the temperature and water diffusion coefficients. $\dot{Q}$ is the mass transfer rate between the liquid and gas water phases and L_v is the mass latent heat of water. $\overline{\theta' u_j'}$, $\overline{q_v' u_j'}$ and $\overline{q_l' u_j'}$ are subgrid fluxes of heat, vapor and liquid water fractions. The subgrid terms are closed in the next section using the eddy-viscosity paradigm.

2.3 Phase transition modelling

It is assumed in the present model (see [*Sommeria*, 1976] for details) that the rate of phase transition is infinitely fast, or equivalently, that the liquid and gas phases are in thermo-chemical equilibrium at every time. Under this assumption, saturation properties provide additional relations between q_v and q_l. The saturation specific humidity is

$$q_v^{sat} = \frac{\epsilon p_{\text{sat}}}{p_0(z) - (1-\epsilon) p_{\text{sat}}}, \tag{5}$$

in which the saturation pressure can be approximated as

$$p_{\text{sat}}(T) = 610.78 \exp\left[17.269 \frac{T - 273.16}{T - 35.86} \right]. \tag{6}$$

and where $\epsilon = R_d / R_v$ is the molecular mass ratio of dry air to that of water.

Under the infinitely fast relaxation approximation, the source term $\dot{Q}$ in Eq. (4) can then be computed from

$$\dot{Q} = \begin{cases} -q_{\text{l}}/\Delta t & \text{if } q_v < q_v^{sat} \text{ and } q_{\text{l}} < \Delta\tilde{q}_v \\ \Delta\tilde{q}_v/\Delta t & \text{otherwise} \end{cases} \tag{7}$$

with [*Grabowski and Smolarkiewicz*, 1990; *Sommeria*, 1976]

$$\Delta\tilde{q}_v = \frac{c_p R_d (\theta_0 \Pi)^2 (q_v - q_v^{sat})}{c_p R_d (\theta_0 \Pi)^2 + \epsilon q_v^{sat} L_{\text{v}}^2 (\frac{\theta_0}{\theta} - \frac{\theta_0}{\theta} \frac{R_d \theta_0 \Pi}{\epsilon L_{\text{v}}})}. \tag{8}$$

Let us now define the virtual temperature θ_v in the buoyancy term as

$$\theta_{\text{v}} = \theta \left[1 - \left(1 - \frac{1}{\epsilon} \right) q_v - q_{\text{l}} \right], \tag{9}$$

2.4 Buoyancy and Coriolis forces

The external force terms like the buoyancy term in Eq. (3b) are incorporated through a body force $F_i = F_{b,i} + F_{c,i}$. Under the Boussinesq approximation, the buoyancy term is given by,

$$F_{b,z} = \frac{g}{\Theta_0}(\theta_v - \Theta_0) \tag{10}$$

The effects of a rotating reference frame on an f plane can be included through the Coriolis force. The acceleration due to the Coriolis force $F_{f,i}$ is computed for the two horizontal velocity components as

$$F_{c,x} = -f(V_g - u_y) \tag{11}$$

$$F_{c,y} = f(U_g - u_x) \tag{12}$$

where U_g and V_g are related to the geostrophic wind. A similar approach is used for all additional force terms considered in the present study, e.g. canopy drag $F_{c,i}$ in Eq. (3b). Specific components canopy drag are discussed in Section 4.5.

2.5 Subgrid modeling

The governing equations of turbulent flows, thermal convection and humidity transport in atmospheric boundary layers are the filtered Navier-Stokes equations. The subgrid terms $\overline{u_i' u_j'}$, $\overline{\theta' u_j'}$, $\overline{q_v' u_j'}$ and $\overline{q_l' u_j'}$ are closed in the present work using the eddy-viscosity paradigm. Therefore, the subgrid fluxes are expressed as

$$\overline{u_i' u_j'} = -\nu_t \left(\frac{\partial u_i}{\partial x_j} + \frac{\partial u_j}{\partial x_i} \right), \tag{13a}$$

$$\overline{\theta' u_j'} = -D_{h,t} \frac{\partial \theta_l}{\partial x_j}, \tag{13b}$$

$$\overline{q_v' u_j'} = -D_{q,t} \frac{\partial q_v}{\partial x_j}, \tag{13c}$$

$$\overline{q_l' u_j'} = -D_{q,t} \frac{\partial q_l}{\partial x_j} \tag{13d}$$

where ν_t, $D_{h,t}$ and $D_{q,t}$ are the subgrid viscosity, subgrid thermal diffusivity, and subgrid humidity diffusivity, respectively. In the classical Smagorinsky approach, the subgrid vis-

cosity is given by,

$$\nu_t = \lambda^2 |S| \tag{14}$$

where $\lambda = (C_S \Delta)$ is a mixing length defined by the Smagorinsky constant C_S and a filter length Δ (taken equal to the grid size in this work) and $|S| = \sqrt{2 S_{ij} S_{ij}}$ is the magnitude of the strain rate tensor,

$$S_{ij} = \frac{1}{2}\left(\frac{\partial u_i}{\partial x_j} + \frac{\partial u_j}{\partial x_i}\right) \tag{15}$$

Since stratification has an effect on subgrid scales of motion and therefore the energy transfer from resolved to subgrid scales, the amplitude of subgrid viscosity must be modified accordingly. This is classicaly done by modifying the subgrid lentghscale [*Deardorff*, 1980; *Moeng*, 1984]. In the case of stable stratification, the eddy viscosity $\nu_t = \lambda^2 f_B |S|$ is reduced by the buoyancy factor f_B.

$$f_B = \begin{cases} 1, & \text{for } N^2 \leq 0 \\ \max[0, \sqrt{1 - \frac{N^2}{Pr_t |S|^2}}\ ], & \text{for } N^2 > 0 \end{cases} \tag{16}$$

where $N^2 = g/\Theta_0 \times \partial\overline{\theta}/\partial z$. For subgrid heat flux in filtered temperature equation, the turbulent thermal diffusivity is related to eddy viscosity through a turbulent Prandtl number

$$K_h = \frac{\nu_t}{D_{h,t}} \tag{17}$$

In this study, the vapor and liquid water fractions are assumed to have the same humidity diffusivity. Following the same analogy, the humidity diffusivity is related to the thermal diffusivity by

$$K_q = \frac{\nu_t}{D_{q,t}} \tag{18}$$

where $D_{q,t}$ is turbulent humidity diffusivity and K_q is turbulent Prandtl number for humidity. Hereafter, ν, D_θ and D_q denote the total viscosity, the total thermal diffusivity and the total humidity diffusivity, respectively. These total diffusivities include both molecular and turbulent parts.

2.6 Surface layers and boundary conditions

2.6.1 Sponge layers

It is worth noting that atmospheric boundary layer simulations frequently use sponge zones to damp spurious wave generation at computational domain boundaries, and that an

external force can also be used for that purpose. The damped solution field is expressed as,

$$\tilde{\phi}(t+\Delta t) = \phi(t+\Delta t) - \sigma_{sponge}(x)\left[\phi(t+\Delta t) - \phi_{target}\right] \tag{19}$$

where ϕ could be density, velocity, temperature, or humidity and ϕ_{target} its corresponding target value, and $\sigma_{sponge}(x)$ is the absorbing strength. The second term in the right hand of (19) correspond to the force to be added,

$$F_{s,i} = \sigma_{sponge}(x)\left(\phi(t+\Delta t) - \phi_{target}\right) \tag{20}$$

The shape of the absorbing strength and target values require some attention. Following [*Xu and Sagaut*, 2013], the following profile of absorbing strength is used in this work,

$$\sigma_{sponge}(x) = \frac{3125(L_{sponge} - x)(x - x_0)^4}{256(L_{sponge} - x_0)^5} \tag{21}$$

where L_{sponge} is the width of the sponge layer, and x_0 is its starting position. On the other hand, the target field ϕ_{target} is often given by the test case specification; if it is not known, it is set equal to an average field calculated at each time step using the method presented in [*Chevillotte and Ricot*, 2016], namely,

$$\overline{\phi}(t+\Delta t) = (1-C)\overline{\phi}(t) + C\phi(t+\Delta t) \tag{22}$$

where C is a small value parameter.

2.6.2 Surface models

Large-Eddy Simulation of atmospheric boundary layer flows requires the use of wall models to account for small scale dynamics in the vicinity of the ground and additional effects such as roughness effects. Most of these models evaluate the surface fluxes of the horizontal momentum components, temperature and humidity using the Monin - Obukhov similarity theory (MOST). The Monin-Obukhov relationships for the bottom boundary are [*Dyer*, 1974],

$$\frac{\kappa z}{u_*}\frac{\partial u}{\partial z} = \phi_m(z/L) \tag{23a}$$

$$\frac{\kappa z}{\theta_*}\frac{\partial \theta}{\partial z} = \phi_h(z/L) \tag{23b}$$

$$\frac{\kappa z}{q_*}\frac{\partial q_t}{\partial z} = \phi_h(z/L) \tag{23c}$$

where $\kappa = 0.41$ is the Von Kármán constant, u_* is the friction velocity, θ_* is the characteristic temperature, q_* is the characteristic humidity, and L is the Obukhov length given by,

$$L = \frac{u_*^2 \theta_0}{\kappa g(\theta_* + 0.61\theta_0 q_*)} \tag{24}$$

The functions ϕ_m and ϕ_h depend on the stability parameter z/L which defines in turn the type of boundary layer. For neutral case $\phi_m = 1$ whereas ϕ_h does not apply because potential temperature is uniform over the domain. For other cases, these functions are given by [*Dyer*, 1974],

$$\text{if } z/L < 0 \quad \phi_m = (1 - 16(z/L))^{-1/4} \tag{25a}$$

$$\phi_h = (1 - 16(z/L))^{-1/2} \tag{25b}$$

$$\text{if } z/L > 0 \quad \phi_m = \phi_h = 1 + 5(z/L) \tag{25c}$$

where $z/L < 0$ for convective case, and $z/L > 0$ for stable case.

Besides, a surface model for turbulent viscosity is necessary to consider the fact that turbulence is damped close to the wall. A blending function is used at the second off-wall node considering the mixing length close to the wall

$$\frac{1}{\lambda^n} = \frac{1}{\lambda_0^n} + \frac{1}{\kappa(z + z_0)^n} \tag{26}$$

where $\lambda_0 = C_S \Delta x$ and n is a free parameter, set to unity in the following simulations.

2.6.3 Boundary conditions

In all simulations, a free-slip condition is used for the top boundary, whereas the Monin-Obukhov wall model is implemented at the bottom boundary. The implementation of Monin-Obukhov formulation depends on the chosen boundary condition in the different stratification situations. Three possible options are available:

1. Both the friction velocity u_* and the characteristic dynamic temperature θ_* are specified when fixed momentum fluxes and a fixed surface heat flux are given. Under these conditions, the Obukhov length can be computed directly from expression (24). Thus, velocities, temperature, stress and heat flux of the first node from wall can be calculated according Monin-Obukhov formulation.

2. The friction velocity u_* is given and surface heat flux is unknown. In this condition, L needs to be retrieved from the implicit relationship of Monin-Obukhov formulation. An iterative procedure is adopted to calculate L with fixed u_*. After L is obtained, L is used to obtain velocities, temperature, stress and heat flux in the same way with the first type.
3. Both the friction velocity u_* and surface heat flux are unknown. In this condition, L needs to be retrieved from the implicit relationship of Monin-Obukhov formulation with two variables. A double loop iterative procedure is adopted to calculate L with variables u_* and θ_*.
4. The treatment on humidity q_t and q_* is the same as the one of potential temperature. Then the vapor and liquid humidities q_v and q_l are calculated by phase transition model.

3 Numerical method: hybrid lattice Boltzmann solver

3.1 The lattice Boltzmann method

3.1.1 basic core

Lattice Boltzmann methods is developed from Lattice Gas Automata [*D'humières and Lallemand*, 1986; *Qian et al.*, 1992; *Chen and Doolen*, 1998] for fluid dynamics. Space and time are classically discretized on a Cartesian grid, whereas particle velocities are discretized on a so-called DdQq lattice (d dimensions and q discrete velocities $c_{i\alpha}$). For the D3Q19 lattice stencil used in this study, the discrete velocities and corresponding weights are given as follows:

$$[c_{\alpha,i},\ w_\alpha] = \begin{cases} [(0,0,0),\ 1/3] & \alpha = 0 \\ [(\pm 1,0,0),(0,\pm 1,0),(0,0,\pm 1),\ 1/18] & \alpha = 1-6 \\ [(\pm 1,\pm 1,0),(\pm 1,0,\pm 1),(0,\pm 1,\pm 1),\ 1/36] & \alpha = 7-18 \end{cases} \tag{27}$$

The flow problem is then solved for $f_\alpha(x_i, t)$, namely the density distribution functions of particles with velocity $c_{\alpha,i}$ at (x_i, t) by the so-called lattice Boltzmann equation. Solution of this equation is usually computed using a second-order accurate Strang splitting, resulting in the definition of a local collision step followed non-local streaming step solved according a Lagrangian scheme:

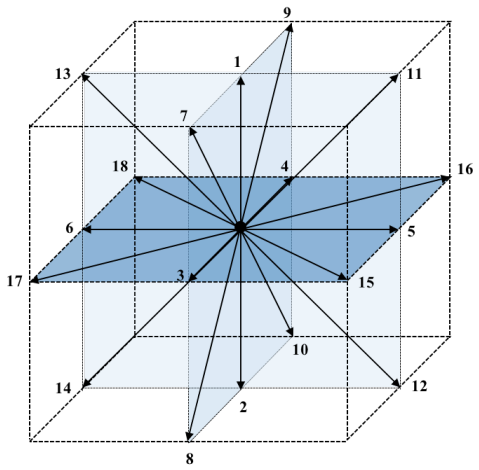

Figure 1. D3Q19 lattice

$$f_\alpha^{coll}(x_i, t) = f_\alpha(x_i, t) + \Omega_\alpha, \tag{28a}$$

$$f_\alpha(x_i, t + \Delta t) = f_\alpha^{coll}(x_i - \Delta t c_{\alpha,i}, t) \tag{28b}$$

The schematic diagram of algorithm of lattice Boltzmann method with collision and

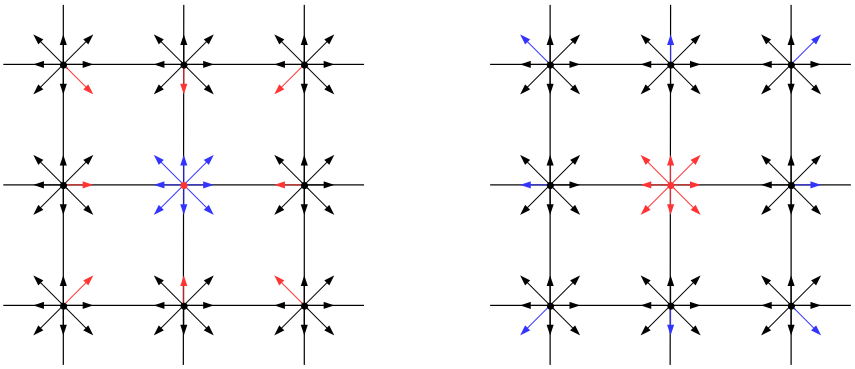

Figure 2. D3Q19 lattice, left: pre-streaming, right: post-streaming

streaming steps are illustrated in Fig. 2. In one time marching loop, the density distribution of particles marked in red advected from the nearest neighbour sites and then collided locally. Following the evolution of distribution functions, the macroscopic quantities such

as density ρ and momentum ρu_i at the time step $t + \Delta t$ are updated by distribution functions in their velocity moments,

$$\rho = \sum_{\alpha} f_{\alpha} \tag{29a}$$

$$\rho u_i = \sum_{\alpha} f_{\alpha} c_{\alpha,i} \tag{29b}$$

For the local collision step, the single relaxation time model (BGK model) [*Qian et al.*, 1992] is widely used because of its simplicity. The original BGK model suffered numerical instability problems in high Reynolds flows [*d'Humières et al.*, 2002]. The BGK collision with regularization exhibits better stability and accuracy properties [*Latt and Chopard*, 2006; *Malaspinas*, 2015; *Coreixas et al.*, 2017; *Mattila et al.*, 2017]. This approach was further improved by *Jacob et al.* [2018], who proposed a dynamic hybrid recursive regularized (HRR) BGK model with self-adaptive dissipation for Large-Eddy Simulation of high Reynolds number flows and Reynolds-Averaged Numerical Simulation [*Wilhelm et al.*, 2018]. Therefore, the hybrid recursive regularized collision model [*Jacob et al.*, 2018] is used in the present work. By using BGK collision model and $f_{\alpha} = f_{\alpha}^{\mathrm{eq}} + f_{\alpha}^{\mathrm{neq}}$, the post-collision distribution function is expressed as

$$f_{\alpha}^{coll}(\vec{x}, t) = f_{\alpha}(\vec{x}, t) - \frac{1}{\tau}(f_{\alpha} - f_{\alpha}^{\mathrm{eq}}) \tag{30a}$$

$$= f_{\alpha}^{eq}(\vec{x}, t) + (1 - \frac{1}{\tau}) f_{\alpha}^{\mathrm{neq}} \tag{30b}$$

$$\approx f_{\alpha}^{eq}(\vec{x}, t) + (1 - \frac{1}{\tau}) \mathcal{R}(f_{\alpha}^{\mathrm{neq}}) \tag{30c}$$

where $f_{\alpha}^{\mathrm{neq}}$ is the non equilibrium function, $\mathcal{R}({f_{\alpha}}^{neq})$ is hybrid recursive regularization on off-equilibrium distribution function. τ is the dimensionless relaxation time which is linked with kinetic viscosity by $\nu = (2\tau - 1)/6$. Subgrid viscosity is implemented in the LBM method by replacing the molecular viscosity by the effective viscosity $\nu_{eff} = \nu + \nu_t$ in this formula, leading to a consistent implementation [*Sagaut*, 2010; *Malaspinas and*

Sagaut, 2012]. The local equilibrium distribution f_α^{eq} is given by

$$
\begin{aligned}
f_\alpha^{eq} = w_\alpha \Big\{ \rho + \frac{c_{\alpha,i}\rho u_i}{c_s^2} + \frac{\mathcal{H}_{\alpha,ij}\mathcal{A}_{ij}^{(0)}}{2c_s^4} + \frac{1}{6c_s^6} \Big[\\
3(\mathcal{H}_{\alpha,xxy} + \mathcal{H}_{\alpha,yzz})(\mathcal{A}_{xxy}^{(0)} + \mathcal{A}_{yzz}^{(0)}) + (\mathcal{H}_{\alpha,xxy} - \mathcal{H}_{\alpha,yzz})(\mathcal{A}_{xxy}^{(0)} - \mathcal{A}_{yzz}^{(0)}) \\
+3(\mathcal{H}_{\alpha,xzz} + \mathcal{H}_{\alpha,xyy})(\mathcal{A}_{xzz}^{(0)} + \mathcal{A}_{xyy}^{(0)}) + (\mathcal{H}_{\alpha xzz} - \mathcal{H}_{\alpha,xyy})(\mathcal{A}_{xzz}^{(0)} - \mathcal{A}_{xyy}^{(0)}) \\
+3(\mathcal{H}_{\alpha,yyz} + \mathcal{H}_{\alpha,xxz})(\mathcal{A}_{yyz}^{(0)} + \mathcal{A}_{xxz}^{(0)}) + (\mathcal{H}_{\alpha,yyz} - \mathcal{H}_{\alpha,xxz})(\mathcal{A}_{yyz}^{(0)} - \mathcal{A}_{xxz}^{(0)}) \Big] \Big\}
\end{aligned}
\tag{31}
$$

where the second order Hermite polynomials $\mathcal{H}_{\alpha,ij} = c_{i,\alpha}c_{j,\alpha} - c_s^2\delta_{ij}$ and $\mathcal{H}_{\alpha,ijk} = c_{i,\alpha}c_{j,\alpha}c_{k,\alpha} - c_s^2[c_\alpha\delta]_{ijk}$ correspond to the second and third order Hermite polynomials with $c_s = \sqrt{1/3}$ being lattice sound speed, $[c_\alpha\delta]_{ijk} = c_{\alpha,i}\delta_{jk} + c_{\alpha,j}\delta_{ik} + c_{\alpha,k}\delta_{ij}$ and δ_{ij} is the classical Kronecker matrix. $\mathcal{A}_{ij}^{(0)} = \rho u_i u_j$ and $\mathcal{A}_{ijk}^{(0)} = \rho u_i u_j u_k$ are respectively the second and third order coefficient of Hermite polynomials.

In large-eddy simulation based on the classical Smagorinsky subgrid model, numerical instability was observed considering only the unfiltered $f_\alpha^{\mathrm{neq}} = f_\alpha - f_\alpha^{\mathrm{eq}}$. An explicit stabilization procedure relying on the combination of f_α^{neq} and its approximation by finite difference solution $f_\alpha^{\mathrm{neq,\,FD}}$ is introduced, leading to the definition of an hybrid recursive regularized collision (HRR [*Jacob et al.*, 2018]) operator. In the HRR collision model, the non-physical modes are filtered by the following hybrid recursive regularization operator:

$$
\begin{aligned}
\mathcal{R}(f_\alpha{}^{neq}) = w_\alpha \Big\{ \frac{\mathcal{H}_{\alpha,ij}\mathcal{A}_{ij}^{(1)}}{2c_s^4} + \frac{1}{6c_s^6} \Big[\\
3(\mathcal{H}_{\alpha,xxy} + \mathcal{H}_{\alpha,yzz})(\mathcal{A}_{xxy}^{(1)} + \mathcal{A}_{yzz}^{(1)}) + (\mathcal{H}_{\alpha,xxy} - \mathcal{H}_{\alpha,yzz})(\mathcal{A}_{xxy}^{(1)} - \mathcal{A}_{yzz}^{(1)}) \\
+3(\mathcal{H}_{\alpha,xzz} + \mathcal{H}_{\alpha,xyy})(\mathcal{A}_{xzz}^{(1)} + \mathcal{A}_{xyy}^{(1)}) + (\mathcal{H}_{\alpha,xzz} - \mathcal{H}_{\alpha,xyy})(\mathcal{A}_{xzz}^{(1)} - \mathcal{A}_{xyy}^{(1)}) \\
+3(\mathcal{H}_{\alpha,yyz} + \mathcal{H}_{\alpha,xxz})(\mathcal{A}_{yyz}^{(1)} + \mathcal{A}_{xxz}^{(1)}) + (\mathcal{H}_{\alpha,yyz} - \mathcal{H}_{\alpha,xxz})(\mathcal{A}_{yyz}^{(1)} - \mathcal{A}_{xxz}^{(1)}) \Big] \Big\}
\end{aligned}
\tag{32}
$$

where $\mathcal{A}_{ij}^{(1)} = \sum_i c_{\alpha,i}c_{\alpha,j}f_\alpha^{neq}$ is the second-order off-equilibrium moment and the third-order off-equilibrium moment is recursively computed by using $\mathcal{A}_{ijk}^{(1)} = u_i\mathcal{A}_{jk}^{(1)} + u_j\mathcal{A}_{ki}^{(1)} + u_k\mathcal{A}_{ij}^{(1)}$. In addition, the off-equilibrium moment is fractionally approximated by its solution in Chapman-Enskog analysis by using $\mathcal{A}_{ij}^{(1,\mathrm{HRR})} = \sigma\mathcal{A}_{ij}^{(1)} + (1-\sigma)\mathcal{A}_{ij}^{(1,\mathrm{FD})}$, where $\mathcal{A}_{ij}^{(1,\mathrm{FD})}$ is given as

$$
\mathcal{A}_{ij}^{(1,\mathrm{FD})} \approx -\Delta t\overline{\tau}\rho c_s^2 \Big[\frac{\partial u_j}{\partial x_i} + \frac{\partial u_i}{\partial x_j} - \frac{2}{3}\frac{\partial u_k}{\partial x_k}\delta_{ij} \Big] \tag{33}
$$

The second-order isotropic central difference scheme is employed to compute the numerical gradient operator. Then, $\mathcal{A}_{ij}^{(1,\mathrm{HRR})}$ is employed in the hybrid recursive regularization Eq. (32). $\sigma \in [0,1]$ is an arbitrary weighting coefficient. In the present simulations, $\sigma = 0.99$ is adopted as a priori value.

297 ### 3.1.2 Implementation of buoyancy, Coriolis and sponge forces

298 The external force terms like the buoyancy term in Eq. (3b) are incorporated through
299 a body force F_α added to the right hand side of Eq. (28). The HRR lattice Boltzmann
300 equation with forcing term is expressed as [see *Feng et al.*, 2019a]

$$f_\alpha^{coll}(x_i,t) = f_\alpha^{eq}(x_i,t) + (1-\frac{1}{\tau})\mathcal{R}(f_\alpha^{\mathrm{neq}}) + F_\alpha \tag{34}$$

301 and the macroscopic density ρ and momentum ρu_i incorporated the general forcing term
302 F_i are updated as

$$\rho = \sum_\alpha f_\alpha \tag{35a}$$

$$\rho u_i = \sum_\alpha c_{\alpha,i} f_\alpha + \frac{\Delta t}{2} F_i \tag{35b}$$

303 where F_i are the components of the external force and the forcing term in HRR-LB equa-
304 tion is expressed as

$$F_\alpha = \left(1-\frac{1}{2\tau}\right)\omega_\alpha \left[\frac{c_{\alpha,i}-u_i}{c_s^2} + \frac{c_{\alpha,j}u_j}{c_s^4}c_{\alpha,i}\right] F_i \tag{36}$$

305 ### 3.1.3 Implementation of boundary conditions

306 In contrast to the conventional CFD methods, an extra step is required for imple-
307 mentation of the boundary condition in the LB method. By using the updated velocities
308 on boundary nodes, the distribution functions on the first off-boundary nodes is recovered
309 via the non-equilibrium reconstruction as follows

$$f_\alpha = f_\alpha^{eq}(\rho,u_i) + f_\alpha^{neq}(\mathcal{A}_{ij}^{(1)},\mathcal{A}_{ijk}^{(1)}). \tag{37}$$

310 where the density at the first off-boundary node is extrapolated from neighbouring nodes.
311 $\mathcal{A}_{ij}^{(1)}$ and $\mathcal{A}_{ijk}^{(1)}$ are computed as

$$\mathcal{A}_{ij}^{(1)} \approx -\Delta t\overline{\tau}\rho c_s^2\big[\frac{\partial u_j}{\partial x_i} + \frac{\partial u_i}{\partial x_j} - \frac{2}{3}\frac{\partial u_k}{\partial x_k}\delta_{ij}\big] \tag{38}$$

312

$$\mathcal{A}_{ijk}^{(1)} = u_i\mathcal{A}_{jk}^{(1)} + u_j\mathcal{A}_{ki}^{(1)} + u_k\mathcal{A}_{ij}^{(1)} \tag{39}$$

313 where the velocity gradients on boundary nodes are computed on these nodes using a
314 first-order biased finite-difference scheme, e.g.

$$\left.\frac{\partial u_y}{\partial x}\right|_b = \frac{1}{\Delta x}(u_{y,b} - u_{y,i}) \tag{40}$$

315 where $u_{y,b}$ is the y component of velocity at boundary.

3.2 Finite volume method for advected scalar quantities

For scalar fields like the total water specific humidity it is possible to use either another set of distribution functions [*Zhang et al.*, 2011] or a hybrid approach in which conservation equations for these quantities are solved using a classical finite volume/finite difference method. The hybrid approach is used here, in order to minimize the number of degrees of freedom per cell of the global method.

The same method is used for all advected scalar quantities (temperature, humidities ...) The convective flux is constructed using MUSCL scheme, while the classical second-order accurate centered difference scheme is adopted for the diffusion term and term of viscous dissipation. The third order MUSCL scheme [*Kim et al.*, 2001] is adopted in this study to preclude spurious wiggles. For example, the x component of the advection term in Eq. (4a) is expressed as

$$u_x \frac{\partial \theta}{\partial x} = u_{x,i} \frac{\theta_{i+1/2} - \theta_{i-1/2}}{\Delta x} \tag{41}$$

$\theta_{i+1/2}$ for instance, can be given as

$$\theta_{i+\frac{1}{2}} = \begin{cases} \theta^L_{i+\frac{1}{2}}, \ u_i > 0 \\ \theta^R_{i+\frac{1}{2}}, u_i \leq 0 \end{cases} \tag{42}$$

and

$$\begin{aligned} \theta^L_{i+\frac{1}{2}} &= \theta_i + \frac{\varphi(r_i)}{4}[(1-\kappa)\delta\theta_{i-\frac{1}{2}} + (1+\kappa)\delta\theta_{i+\frac{1}{2}}], \\ \theta^R_{i+\frac{1}{2}} &= \theta_{i+1} - \frac{\varphi(r_{i+1})}{4}[(1-\kappa)\delta\theta_{i+\frac{3}{2}} + (1+\kappa)\delta\theta_{i+\frac{1}{2}}], \end{aligned} \tag{43}$$

where $\kappa = 1/3$, and,

$$\begin{aligned} &\delta\theta_{i+\frac{1}{2}} = (\theta_{i+1} - \theta_i), \delta\theta_{i-\frac{1}{2}} = (\theta_i - \theta_{i-1}), \\ &\delta\theta_{i+\frac{3}{2}} = (\theta_{i+2} - \theta_{i+1}), \delta\theta_{i-\frac{3}{2}} = (\theta_{i-1} - \theta_{i-2}), \\ &r_i = \frac{\theta_i - \theta_{i-1}}{\theta_{i+1} - \theta_i} \end{aligned} \tag{44}$$

where i represents index of grid rather than lattice discrete velocity. The van Albada limiter function $\varphi(r) = 2r/(1+r^2)$ is used to avoid spurious oscillations [*Hirsch*, 2007].

Besides, the diffusion term is approximated by calculating gradient by a central difference scheme.

$$\begin{aligned} &\frac{\partial}{\partial x}(D_\theta \frac{\partial \theta}{\partial x}) = \frac{1}{\Delta x}\left[D_{\theta,i+1/2}\frac{\theta_{i+1} - \theta_i}{\Delta x} - D_{\theta,i-1/2}\frac{\theta_i - \theta_{i-1}}{\Delta x}\right], \\ &D_{\theta,i+1/2} = \frac{1}{2}(D_{\theta,i} + D_{\theta,i+1}), \ D_{\theta,i-1/2} = \frac{1}{2}(D_{\theta,i} + D_{\theta,i-1}) \end{aligned} \tag{45}$$

where D_θ is total diffusivity of potential temperature and and the same expressions are used to solve for y and z directions.

3.3 Immersed Boundary approach for complex geometries

The present LBM-LES tool is augmented via implementation of Immersed Boundary approach to handle arbitrary geometries while using embedded Cartesian grid. The previous boundary conditions for solid surfaces are implemented in a local reference frame associated to the solid surface in the following way.

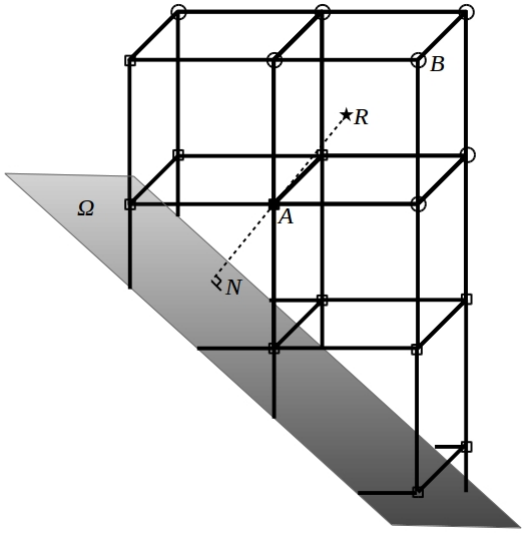

Figure 3. Immersed solid boundary in three-dimension.

Typically, the variables on boundary node A that will enforce a Dirichlet boundary condition for the wall model has to be computed. First, two references points (N and R) are defined and arranged, which are located on the normal line to the wall passing through the boundary node A as described in Fig. 3. N is the intersection point of immersed solid surface Ω and the normal line. R is the reference point with $\overline{NR} = 2.5\Delta x$ distance away from point N. The macroscopic values on point R are interpolated from the neighbors of $\circ$ by using the Shepard's Inverse Distance Weighting (IDW) method [*Shepard*, 1968].

$$\phi(x_i) = \sum_{j=1}^{N} \frac{d(x_i, x_j)^{-p}}{\sum_{j=1}^{N} d(x_i, x_j)^{-p}} \phi(x_j), \tag{46}$$

$$d(x_i, x_j) = \sqrt{(x_j - x_i)^2 + (y_j - y_i)^2 + (z_j - z_i)^2} \tag{47}$$

where $d(x_i, x_j)$ denotes the distance between point x_i and its neighbor x_j. The exponent index p is a free parameter in the IDW method and $p = 2$ is typically recommended [*Gao*

et al., 2007] and adopted in the present implementation. Once the variables of reference point R are computed, the wall models can be implemented in the local reference frame. Details of implementation of boundary conditions, including the coupling with wall models for turbulent flows, are available in Refs [*Wilhelm et al.*, 2018; *Feng et al.*, 2019b].

4 Benchmarking: HRRLB-LES solver for ABLs

4.1 Neutral Boundary Layer

Atmospheric boundary layer under neural condition proposed in the cross-comparisons of [*Andren et al.*, 1994] with slight modifications is used to accessed the LBM-LES solver. We use here a simulation domain of 1280 m×1280 m×1500 m as in [*Chow et al.*, 2005]. Periodic conditions are employed in the horizontal direction, and the roughness length for Monin-Obukhov similarity is set as $z_0 = 0.1$ m. The atmospheric boundary flow is driven by a large scale pressure gradient which results from the balance with a geostrophic wind of $(U_g, V_g) = (10, 0)$ m s^{-1}. The following force is introduced through a source term in the lattice Boltzmann equation (see Eq. 36),

$$F_{c,x} = -f(V_g - u_y) \tag{48a}$$

$$F_{c,y} = f(U_g - u_x) \tag{48b}$$

where the Coriolis parameter is $f = 10^{-4}\text{s}^{-1}$. Simulation was initialized with a reference density of $\rho_0 = 1$ kg m^{-3}, and the analytical Ekman profile for velocity given by [*Cushman-Roisin and Beckers*, 2009]

$$u_x = U_g\,(1 - \exp(-z/H)\cos(z/H)) \tag{49a}$$

$$u_y = U_g \exp(-z/H)\sin(z/H) \tag{49b}$$

where H is the domain height which corresponds approximately to the boundary layer height. The numerical simulation was performed over thirty dimensionless time periods tf as in [*Chow et al.*, 2005]. Two different grids were used with $\Delta x = 32$ m, $\Delta x = 24$ m, and average results were taken over the last six periods that correspond approximately to the inertial oscillation period $2\pi/f$.

Figure 4 shows the mean velocity profile compared with the results of [*Senocak et al.*, 2007]. The mean velocity is averaged in the horizontal plane direction and in time period, and it is normalized with u_*. The numerical results of finer mesh have a better agreement with the reference values. On the whole, it can be observed that even though grid is coarse, the LBM with Smagorinsky model can well predict the flow structures.

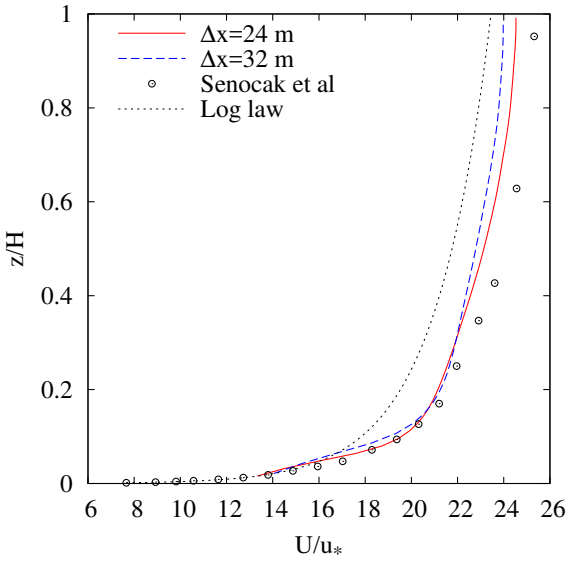

Figure 4. Mean velocity profile (neutral case).

The friction velocity is crucial in prediction of fluid flow in atmospheric boundary layer. Table 1 compares the values of friction velocity obtained in this work with those from the intercomparison [*Andren et al.*, 1994]. Quantitatively speaking, quite consistent results on difference grid resolutions are obtained by our LB model. From the above observation, accuracy and compatibility of the wall model for neutral boundary layer is well proven in our simulations.

To obtain a more intuitive comparison, the normalized stresses obtained from time statistic of the neutral atmospheric boundary layer are compared with reference values is plotted in Fig. 5. With the increasing grid resolution, the results gradually close to total stress in reference, which implies the good grid convergence feature of the present LBM-LES solver.

386 **Table 1.** Friction velocity (neutral case).

	u_* (m/s)
$\Delta x = 24m$ (Smag)	0.437
$\Delta x = 32m$ (Smag)	0.439
Andren/Moeng	0.425
Mason/Brown bsct	0.448
Mason/Brown nbsct	0.402
Nieuwstadt	0.402
Schumann/Graf	0.425

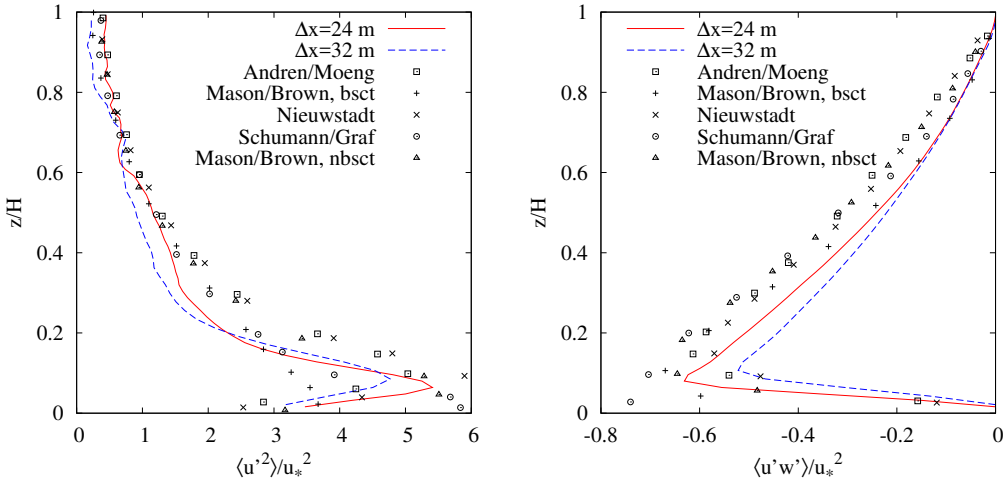

392 **Figure 5.** momentum flux (neutral case).

393 4.2 Stable Boundary Layer

394 The stable atmospheric boundary layer (SBL) is considered the most challenging
395 case for LES because eddies are smaller than in the neutral case; therefore, the resolved
396 turbulence is harder to maintain if the grid is not fine enough. Here we simulate the SBL
397 proposed in the intercomparison of [*Beare et al.*, 2006]. It consists of a 400 m ×400 m
398 ×400 m domain where the flow is driven by a a geostrophic wind of $U_g = 8$ m s^{-1},
399 $V_g = 0$ m s^{-1} and Coriolis parameter of $f = 1.39 \times 10^{-4}$ s^{-1}. Periodic boundary con-
400 ditions are applied in the horizontal directions. At the top boundary, a free slip condition
401 is applied along with a sponge layer over the last 100 m. Monin-Obukhov relationships

with a roughness length of $z_0 = 0.1$ m and a surface cooling of 0.25 K h^{-1} are applied to the bottom boundary.

The initial velocity profile is a constant velocity in the horizontal direction equal to the geostrophic values $u_x = U_g$, $u_y = V_g$ and zero vertical velocity. The initial temperature profile is set as,

$$\theta = \begin{cases} 265 \text{ K} & z \le 100 \text{ m} \\ \theta = 265 + (z - 100)\,\Gamma \text{ K} & z > 100 \text{ m} \end{cases} \tag{50}$$

where $\Gamma = 0.01$ K m^{-1} is a constant slope of potential temperature from height of 100 m to the top of the domain. Initially, a random perturbation of 0.1 K is applied below 50 m is to trigger the turbulence flow.

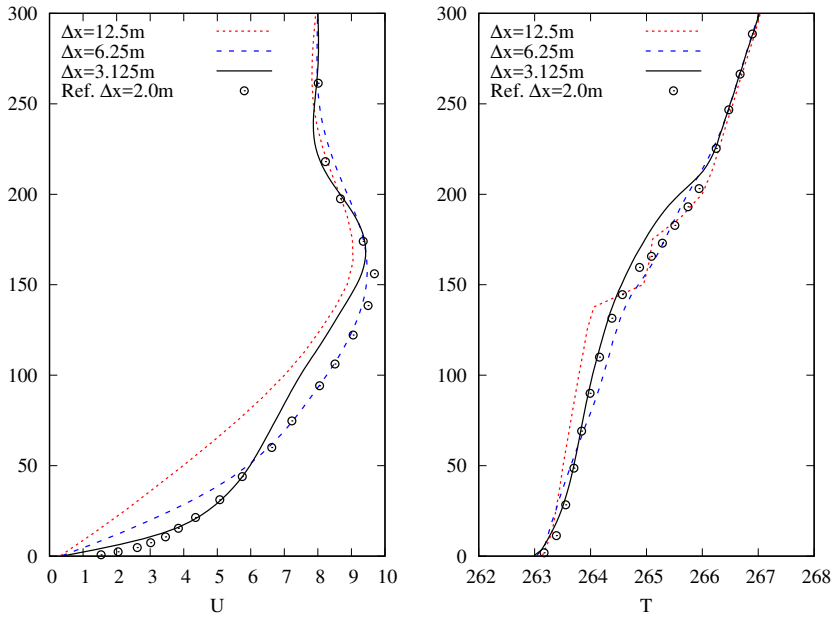

Figure 6. Mean velocity and temperature (stable case). The results were averaged on the 9th hour and compared with the reference data in [*Heerwaarden et al.*, 2017].

Simulations were performed using 3.125, 6.25 m and 12.5 m grids with subgrid model. Smagorinsky constant of $C_S = 0.23$ for subgrid model was suggested in [*Beare et al.*, 2006] by sensitivity analysis is too large for the 6.25 m resolution in our study, thus it is set to $C_S = 0.15$ and used the same value for the 3.125 and 12.5 m grids.

The numerical simulation time was set as 9 h, and results were averaged over the last hour. Figure 6 shows mean profiles of velocity and potential temperature compared

418 to the results with 2.0 m mesh in the intercomparison [*Heerwaarden et al.*, 2017]. Results
419 by the present LBM-LES solver well reproduced the supergeostrophic jet characteristic of
420 stable layers. Temperature profile on Fig. 6 have a good agreement with references values
421 at the bottom of the boundary layer, and the inversion layer takes place at a little higher
422 altitude.

423 4.3 Convective Boundary Layer

424 The convective boundary layer case is taken from [*Nieuwstadt et al.*, 1993] who con-
425 ducted an intercomparison of large-eddy codes from four research groups. The simulation
426 domain is 6400 m×6400 m×2400 m to which we add a sponge layer of 600 m, so the
427 total domain height in our study is 3000 m. The roughness length used for the Monin-
428 Obukhov relationships is $z_0 = 0.16$ m.

429 The convective boundary layer are set in terms of temperature and convective veloc-
430 ity scales defined by,

$$w_* = \left(\frac{g}{T_0} Q_s z_i\right)^{1/3}, \; T_* = \frac{Q_s}{w_*} \tag{51}$$

431 where g is the gravity, T_0 is a reference temperature, Q_s is the surface temperature flux,
432 and z_i is the boundary layer height. As the boundary height is not known *a priori*, an ap-
433 proximate boundary height of $z_{i0} = 1600$ m is used to define initial conditions. The sur-
434 face is heated by a constant temperature flux of $Q_s = 0.06$ K m s^{-1}. Considering Q_s,
435 z_{i0}, and a reference temperature $T_0 = 300$ K, the convective velocity and temperature
436 scales are $w_{*0} = 1.46$ m s^{-1} and $T_{*0} = 0.041$ K. A time scale derived from z_{i0} and w_{*0}
437 is $t_{*0} = 1096$ s. With these scalings, the initial conditions are given by,

For $z \leq z_{i1} = 0.844 z_{i0}$

$$\theta = T_0 + 0.1 r \left(1 - \frac{z}{z_{i1}}\right) T_{*0} \tag{52a}$$

$$u_z = 0.1 r \left(1 - \frac{z}{z_{i1}}\right) w_{*0} \tag{52b}$$

$$u_x = u_y = 0 \tag{52c}$$

For $z > z_{i1}$

$$\theta = T_0 + (z - z_{i1})\,\Gamma \tag{53a}$$

$$u_x = u_y = u_z = 0 \tag{53b}$$

where r is a random number uniformly distributed between -0.5 and 0.5, and $\Gamma = 0.003$ K m^{-1} is a constant temperature gradient over the boundary layer. Simulations were performed for eleven time periods $11t_*$, and averaged results are calculated on the last one hour.

The research groups that participated in the intercomparison of [*Nieuwstadt et al.*, 1993] used different parameters for discretization and subgrid model. Some of them used non uniform grids, so their vertical meshes ranges from 20 m to 60 m. Two of the groups reported a Smagorinsky constant of $C_S = 0.18$ and turbulent Prandtl of $Pr = 0.33$ even though subgrid model differs among them. We decided to use these values in our simulations, and a uniform mesh with two resolutions of $\Delta x = 50$ m and $\Delta x = 25$ m.

The average temperature profile by our LBM-LES solver is plotted in Fig. 7. We compare here our results with that from [*Schmidt and Schumann*, 1989] where averages are taken at $6t_*$, since the temperature profiles were not given in [*Nieuwstadt et al.*, 1993]. A common characteristic of the convective boundary layer is that mean temperature is roughly constant in the mixed layer, approximately the zone between 0.1 and 0.9 z/z_{i0}. This characteristic is well satisfied with the $\Delta x = 25$ m and $\Delta x = 50$ m mesh sizes.

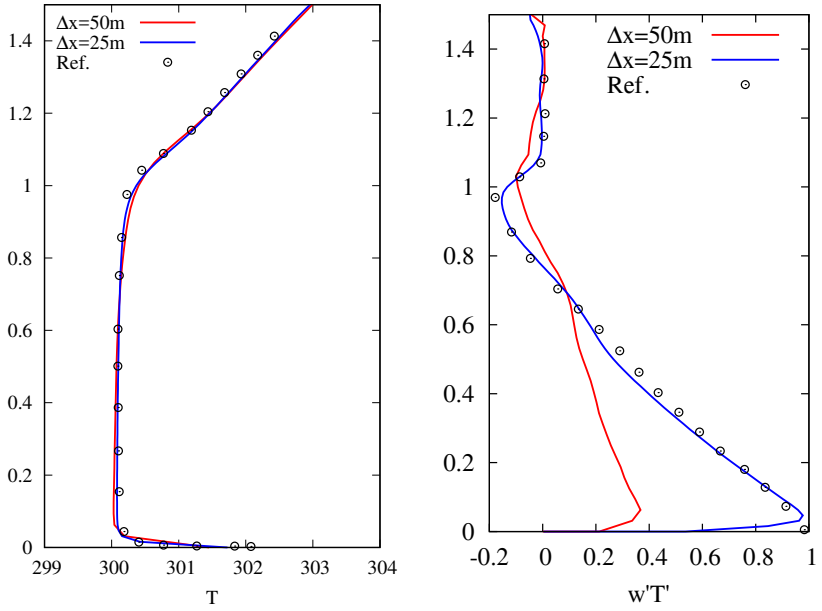

Figure 7. Mean temperature at $6t_*$ and resolved vertical heat flux at $6.5t_*$ (convective case).

Figure 7 also shows the profile of vertical turbulent heat flux. The boundary layer height is defined as the height where this flux reaches its minimum value; this minimum value is known as the entainment flux $-\langle w'\theta'\rangle$. In general, our simulations give smaller values for the entrainment flux and higher values of boundary height than those in [*Nieuwstadt et al.*, 1993].

4.4 Shallow Cumulus Convection

A shallow cumulus convection is simulated by the LBM-LES solver to evaluate the moist thermodynamics and its interaction with subgrid modeling. The shallow cumulus convection simulations follows the setup of the Barbados Oceanographic and Meteorological Experiment (BOMEX) model inter-comparison case [*Siebesma et al.*, 2003]. This is the most prevalent shallow cumulus LES case. Siebesma and Cuijpers [*Siebesma and Cuijpers*, 1995] conducted a early large-eddy simulation based on a case from the BOMEX field experiment.

In this case, a height dependent geographic wind u_g is given by a linear formula $u_g = (-10 + 1.8 \times 10^{-3} z)$ m s^{-1} and the Coriolis parameter is set to $f = 0.376 \times 10^{-4}$s^{-1}. The initial conditions for velocity, liquid water potential temperature and total water mixing ratio are linear profiles following the values given on Table 2.

The temperature and humidity surface fluxes are 8×10^{-3} K m s^{-1} and 5.2×10^{-5} m s^{-1}, respectively. The shear stresses are prescribed by $\overline{u_i w} = -u_*^2 u_i/(u_1^2 + u_2^2)^{1/2}$, with $u_* = 0.28$ m s^{-1}.

Table 2. Initial conditions for cumulus case

Height (m)	q_t (g kg^{-1})	θ_l (K)	u (m s^{-1})	v (m s^{-1})
0	17.0	298.7	-8.75	0
520	16.3	298.7		
700			-8.75	
1480	10.7	302.4		
2000	4.2	308.2		
3000	3.0	311.85	-4.61	0

476 Moreover, additional terms are added to represent the large-scale forcing which
477 could not be represented directly in the LES. The source terms of momentum conserva-
478 tion equations, temperature equation and water equations are parameterized considering
479 the effects of large-scale subsidence, radiative cooling and moisture effects. Their details
480 are described in [*Siebesma et al.*, 2003].

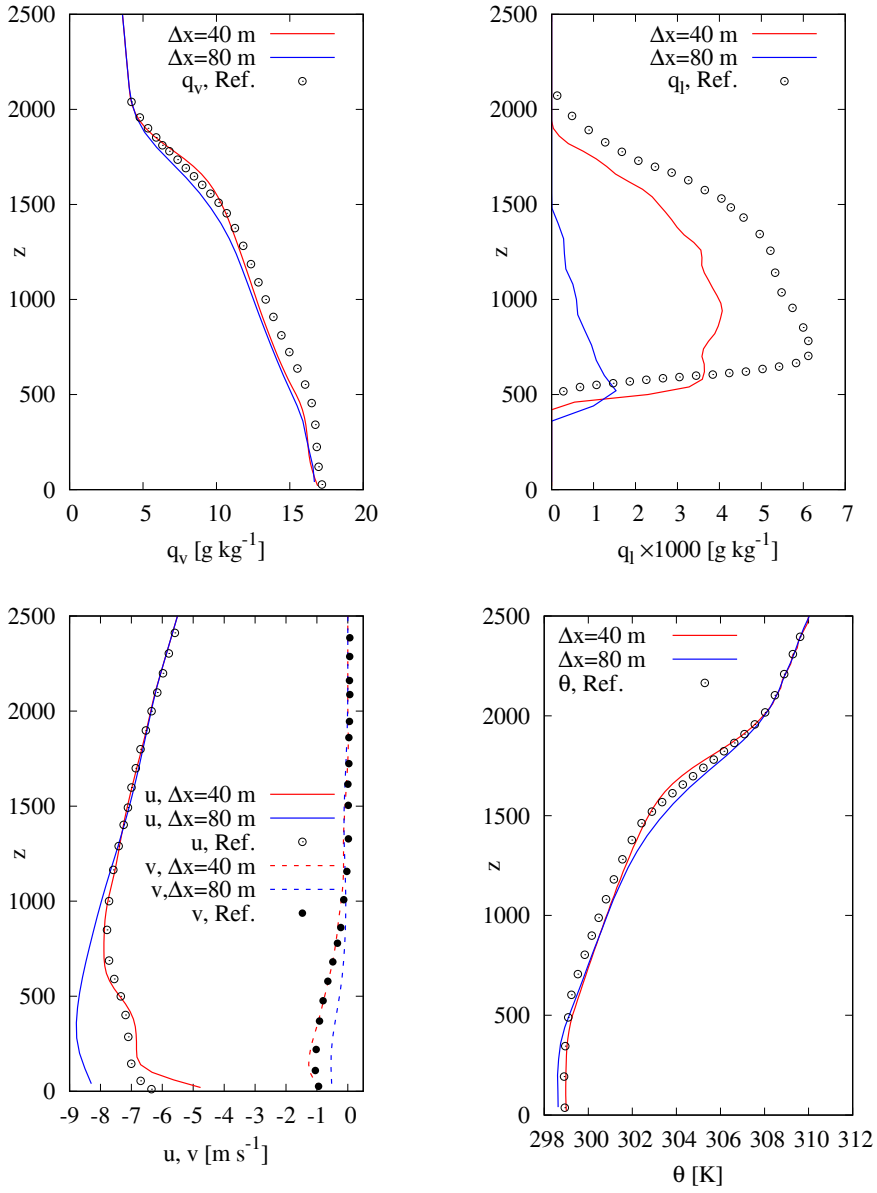

481 **Figure 8.** Mean profiles (convective cumulus case).

482 The LBM-LES solver with condensation scheme has been employed to reproduce
483 the case at two resolutions of Δx = 80 m and 40 m in domain of 5000 m×5000 m×3000

m. Time interval is 0.54s on coarse mesh and 0.27s on fine mesh, respectively. Smagorinsky constant of $C_S = 0.23$ and turbulent Prandtl of $Pr = 0.33$ is adopted both for potential temperature and water equations. Small random perturbations are applied to initiate turbulence, and both of the simulations are run for six hours. Statistics are performed during the final hour.

Figure 8 shows profiles of turbulence statistics from the simulations. All of the results are in good agreement with the reference data from [*Siebesma et al.*, 2003]. Consistent results are clearly obtained with comparison of data from coarse mesh and fine mesh. The mean profiles of velocities, potential temperature, vapor water and liquid water on fine mesh are confirmed closely to reference values. The mixed region below the surface of 540 m is well captured, which has valid the accuracy of wall model with complex moist thermophysics. Furthermore, the conditionally unstable layer from 540 m to 1500 m, and the inversion layer from 1500 m to 2000 m are also clearly observed in the results.

4.5 Neutral, stable and convective atmospheric boundary layer with canopy effects

The present LBM-LES method is further assessed considering the flows in neutral, stable and convective boundary layer over a forest canopy. In this configuration, the forest is modeled as a non-uniform homogenized porous medium. The forest model is implemented as a volumetric source term in both the macroscopic momentum and temperature equations. More precisely, altitude-dependent drag force and heat release source term are introduced within the forest. This heat source is assumed to be proportional to solar radiation; therefore, it achieves the largest value at the canopy top and diminishes exponentially through it with an extinction coefficient $\gamma = 0.6$,

$$S_\theta = \frac{\partial}{\partial z}\left(Q_h \exp(-\gamma A_c)\right) \tag{54}$$

The canopy-top heat flux Q_h is prescribed as a constant value that defines the type of stability, namely a positive source for convective case, a negative source for stable case, and no source for the neutral case. The values studied in this section are, 1) Neutral BL: $Q_h = 0.0$ K m s^{-1}, 2) Convective BL: $Q_h = 0.015$ K m s^{-1}, and 3) Stable BL: $Q_h =$

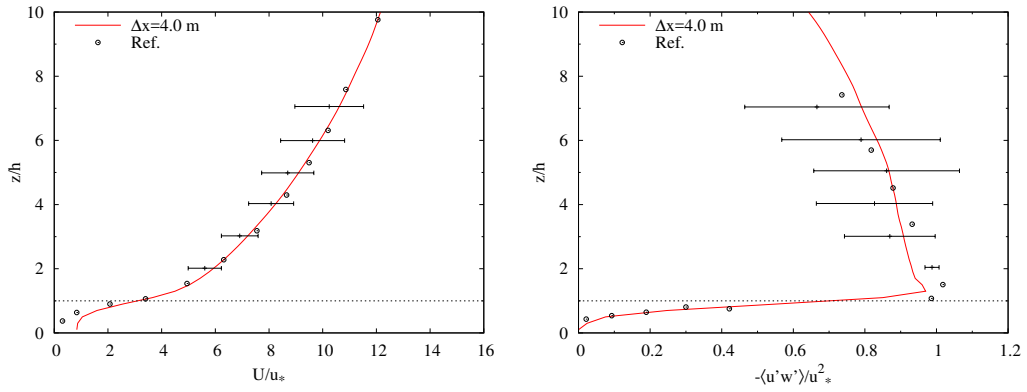

(a) Mean velocity profile. (b) Resolved vertical momentum flux.

Figure 9. Mean longitudinal velocity profile (left) and resolved turbulent shear stress (right) predicted by the present LB-LES method in neutral boundary layer with canopy effect.

-0.0035 K m s^{-1}. The downward cumulative leaf-area index A_c in Eq. (54) is given by,

$$A_c = \int_z^h a_f dz \tag{55}$$

The leaf-area density a_f is related to the forest profile. *Nebenführ and Davidson* [2015] used an empirical profile, while a beta probability distribution profile is used by [*Markkanen et al.*, 2003]. The later solution is used in the present work, with parameters $\alpha = 3$ and $\beta = 2$ as in [*Banerjee et al.*, 2017], leading to

$$a_f\left(\frac{z}{h}\right) = \frac{\left(\frac{z}{h}\right)^2\left(1-\frac{z}{h}\right)}{\int_0^1 \left(\frac{z}{h}\right)^2\left(1-\frac{z}{h}\right) d\left(\frac{z}{h}\right)} \tag{56}$$

Note that this is a dimensionless expression, which can be adapted to different forest parameters. Thus, using the same leaf-area index LAI=4.3 as [*Nebenführ and Davidson*, 2015], the dimensional value of leaf-area density is obtained through $a_f(z) = (LAI/h)a_f(z/h)$.

The forest is assumed to be horizontally homogeneous with a drag coefficient of $C_D = 0.15$. The drag force is finally evaluated as

$$F_{f,i} = -C_D a_f(z) U u_i \tag{57}$$

Results are compared with the Navier-Stokes based reference LES simulations and field measurements from a forested region in the south-east of Sweden reported in [*Nebenführ and Davidson*, 2015]. The computational domain size is 400 m×400 m×400 m with a canopy of height $h = 20$ m. The flow is driven by a geostrophic wind such as $U_g = 5$

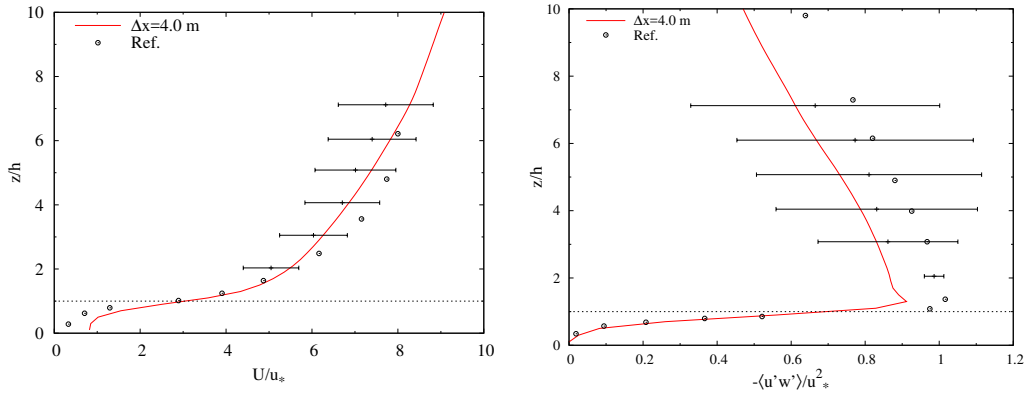

(a) Mean velocity profile. (b) Resolved vertical momentum flux.

Figure 10. Mean longitudinal velocity profile (left) and resolved turbulent shear stress (right) predicted by the present LB-LES method in convective boundary layer with canopy effect.

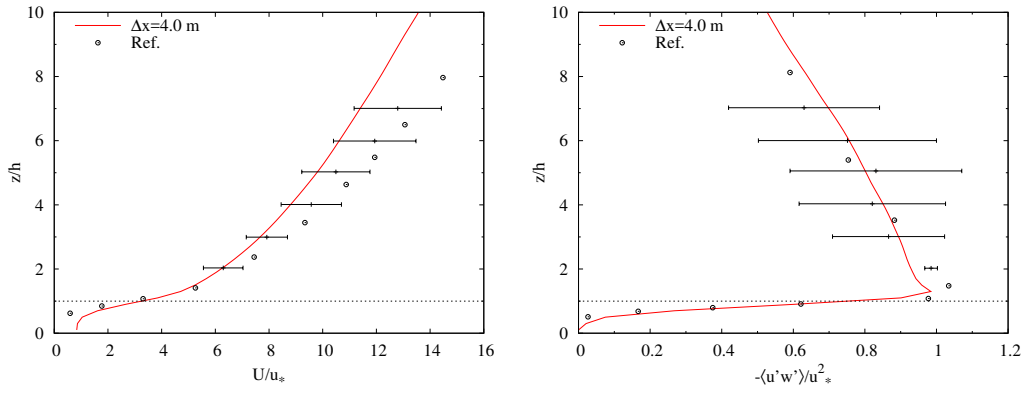

(a) Mean velocity profile. (b) Resolved vertical momentum flux.

Figure 11. Mean longitudinal velocity profile (left) and resolved turbulent shear stress (right) predicted by the present LB-LES method in stable boundary layer with canopy effect.

m s^{-1}, $V_g = 0$ m s^{-1}, and the Coriolis parameter is set equal to $f = 1.22 \times 10^{-4}$ s^{-1}. The initial temperature is uniform, with $\theta = 300$ K. Lateral boundaries are periodic, a free slip condition with a sponge layer of thickness 50 m is imposed on the top boundary , and while bottom boundary is assumed to be adiabatic with Monin-Obukhov relationships for velocity. The simulations were performed over 3 h of physical time, and results were averaged over the last hour. A uniform grid with $\Delta x = 4$m with $\Delta t = 0.03$s as applied in the simulation within the canopy.

Results for the neutral case are displayed in Fig. 9. The field measurements uncertainties are represented with error bars. Note that the lowest field measurements were taken at $z/h \approx 2$; therefore, the results are normalized with friction velocity calculated at the same height, i.e.

$$u_* = \left(\langle u'w' \rangle^2 + \langle v'w' \rangle^2 \right)^{1/4}$$

A very good agreement is observed on both the mean velocity profile and the resolved shear stress profile.

Results obtained in the convective and stable cases are shown in Fig. 10, and Fig. 11, respectively. The velocity profiles exhibit a good agreement with field measurements and simulations for the convective case, and also show an excellent agreement for the stable case. It is worth noting that the stable case shows however smaller velocities above the canopy.

Resolved vertical momentum fluxes in convective and stable ABL with canopy effects are presented in Fig. 10(b) and 11(b), respectively. Results are within the range of field measurements above $z/h = 3$ but deviate at $z/h = 2$.

The resolved turbulent vertical heat flux is shown in Fig. 12. An excellent agreement between the present results and reference data is obtained both in convective case and stable case. In general, the present simulations give smaller values on the resolved flux in top region for stable ABL, a phenomena that might be due to the use of a sponge layer to prevent the growth of spurious wiggles and waves.

5 Benchmarking: Complex urban flows

The last illustrations of the capabilities of the present LBM-LES simulation tool deal with urban flows in complex geometries. The first case deals with the prediction of wind

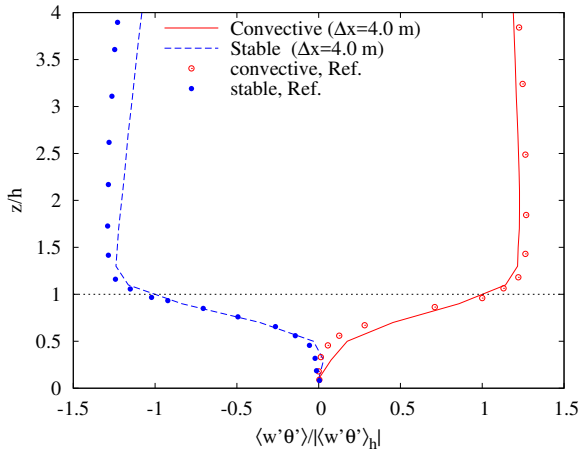

553 **Figure 12.** Resolved vertical heat flux (convective and stable canopy).

562 in realistic urban areas, while the second is related to atmospheric dispersion of pollutant
563 in urban areas.

564 ### 5.1 Wind prediction in Shinjuku district in Tokyo

565 The first test case for urban flow prediction deals with the prediction of urban wind
566 conditions, including wind gusts for evaluation of pedestrian comfort in the Shinjuku dis-
567 trict in Tokyo [*Jacob and Sagaut*, 2018].

568 This configuration belongs to the data basis of the Architectural Institute of Japan.
569 An area of $1km^2$ is selected, including all buildings, in which mean wind field measure-
570 ments are available for the sake of validation. The case of North wind is selected for the
571 sake of illustration.

572 A computational domain of size $4600m \times 5000m \times 1500m$ is defined. Different
573 grid resolutions have been considered. In the coarse grid, medium and fine grid cases,
574 the smallest mesh size near solid surfaces is taken equal to $2m$, $1m$ and $0.5m$, respectively.
575 The total number of grid points ranges from 22×10^6 (coarse grid) to 136×10^6 (fine grid)
576 with a value of 54×10^6 for the medium grid case.

577 Location of probes used for field measurements and comparisons with LBM-LES re-
578 sults are displayed in Figure 13, showing that at all probe locations (except one) numerical
579 results are within measurement uncertainties.

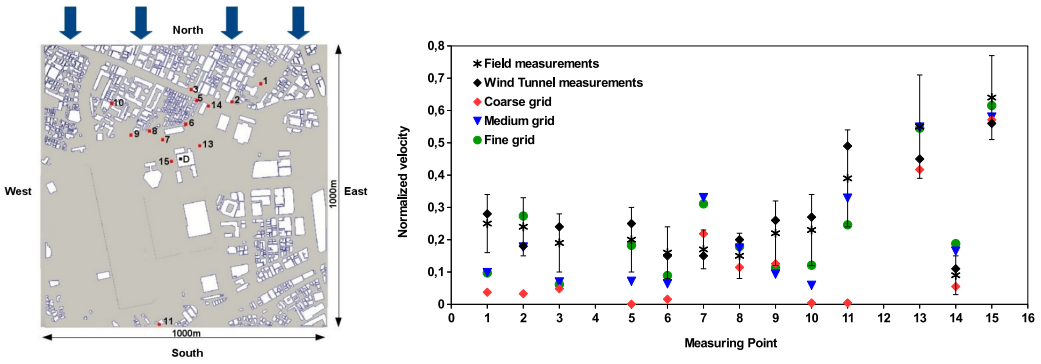

(a) Position of measurements points.

(b) Normalized mean velocities.

Figure 13. Locations of the probes inside Tokyo Shinjuku district used for in situ field measurements (left) and simulated normalized velocities compared with wind tunnel and fields measurements (right). Vertical bars are related to experimental uncertainties.

5.2 Pollutant dispersion in Paris

The capability of the LBM-LES tool to predict the dispersion of a gaseous pollutant in complex urban areas is now illustrated. For the sake of validation, the MODITIC data basis is used [*Robins et al.*, 2016; *Merlier et al.*, 2019].

The present configuration corresponds to the dispersion of a neutral gas released on the ground at a constant rate in the "Avenue des Champs Elysées" district in Paris, for which wind tunnel data have been produced. The main wind direction and the pollutant source location are shown in Figure 14, and results shown here are related to Configuration 1. The smallest mesh size is taken equal to $H/45$, where H is the mean building height, leading to a total number of grid points equal to 175×10^6 for the configuration 1.

The normalized mean pollutant concentration obtained in both wind tunnel experiments and LBM-LES simulations are displayed in Figure 15. It is observed that very satisfactory results are obtained, including in small streets crossing the main avenue. This last observation shows that a reliable prediction of transverse diffusion in urban areas is obtained.

6 Conclusion

We have described a new tool for LES of atmospheric flows in this paper. Large eddy simulation (LES) with the lattice Boltzmann method (LBM) was used to simulate

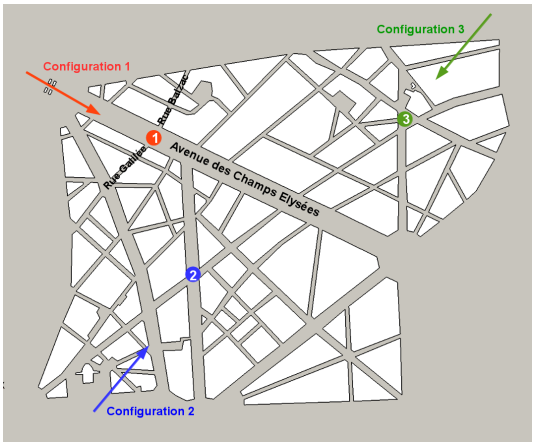

598 **Figure 14.** Visualisation of the simulated area around the "Avenue des Champs Elysées". Configuration 1
599 is selected in the present article.

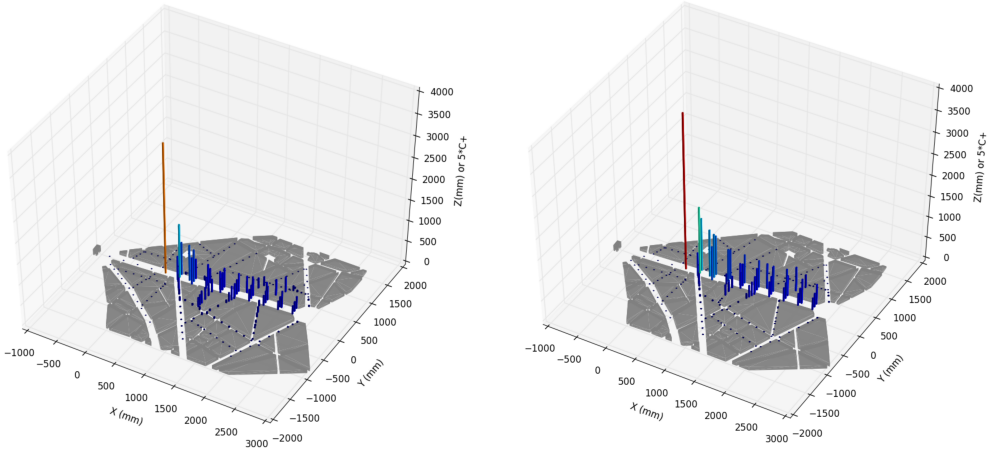

(a) Experimental data. (b) Numerical data.

600 **Figure 15.** Visualisation of the normalized concentration obtained for dispersion of a neutral gas around the
601 "Avenue des Champs Elysées".

605 dry and cloudy atmospheric boundary layers (ABL), along with flows in complex urban
606 areas. The subgrid model for the LES was the classical Smagorinsky model with a given
607 constant. For dry ABL we used mass, momentum, and potential temperature as governing
608 equations, whereas for cloudy ABL, in addition to mass and momentum, we used liquid
609 and vapor water specific humidities and potential temperature equations. Total water spe-
610 cific humidity is the sum of water vapor and liquid water humidities, and condensation
611 occurs when total water exceeds saturation value. Governing equations were solved by the

LBM and by using a finite volume scheme for potential temperature and water specific humidities.

To validate our LBM-LES solver, we first simulated the four basic ABL cases coming from previous intercomparison of LES codes. These were the neutral [*Andren et al.*, 1994; *Chow et al.*, 2005; *Senocak et al.*, 2007], convective [*Schmidt and Schumann*, 1989; *Nieuwstadt et al.*, 1993], stable [*Beare and Macvean*, 2004; *Beare et al.*, 2006], and cloudy convective boundary layer [*Siebesma et al.*, 2003]. Then three extra cases for ABL with canopy effects were performed by our solver. The altitude-dependent drag force and heat release source term were introduced and assessed in the present solver compared reference data in [*Nebenführ and Davidson*, 2015] .

For the neutral case, Coriolis force was added to the LBM, and simulations were performed with $\Delta x = 24$ m and $\Delta x = 32$ m meshes. This case was very sensitive to subgrid model, and only results with subgrid model were satisfactory and presented in the paper. Mean velocity profile, friction velocity and Reynolds stresses predicted in our simulations were in good agreement with literature results. For the convective case, we performed the numerical simulation on $\Delta x = 25$ m and $\Delta x = 50$ m grids with subgrid model. Average temperature profile with subgrid model shows very good agreement with literature results. For stable boundary layer, we used $\Delta x = 3.125$ m, $\Delta x = 6.25$ m and $\Delta x = 12.5$ m meshes with subgrid model. Mean velocity profile were well reproduced the supergeostrophic jet typical of stable layers. THe mean profile of velocity and temperature were in a good agreement with references values.

In assessment of condensation scheme and interaction of forcing terms: condensation, large scale forcing, a low level drying, and radiative cooling, the cumulus cloud case was considered by the LBM-LES solver. Very good agreement was obtained for mean velocity, liquid water potential temperature, and vapor water specific humidity on $\Delta x = 40$ m and $\Delta x = 80$ m meshes with subgrid model. Liquid water compares very good to the reference result on the finer mesh, but yields pretty small values on the coarser mesh.

The present LBM-LES method was further assessed considering the flows in neutral, stable and convective boundary layer over a forest canopy. The forest was modeled as a non-uniform homogenized porous medium and implemented as a volumetric source term in both the macroscopic momentum and temperature equations. In general, excellent

643 agreements between the present results and reference data were obtained in neutral con-
644 vective case and stable ABLs with forest canopy effects.

645 At last, the LBM-LES tool was succesfully assessed considering two urban flow
646 configurations: wind prediction in Shinjuku district in Tokyo, and gaseous pollutant dis-
647 persion in the Champs Elysées district in Paris. In both cases, very satisfactory compar-
648 isons with experimental data were recovered.

649 **Acknowledgments**

650 This work was granted access to the HPC resources of Aix-Marseille Université financed
651 by the project Equip@Meso (ANR-10-EQPX-29-01) of the program “Investissements
652 d’Avenir" supervised by the Agence Nationale de la Recherche. This work was performed
653 using HPC resources from GENCI-TGCC/CINES (Grant 2018-A0052A07679). This work
654 was also supported by project of ProLB software (http://www.prolb-cfd.com). The ProLB
655 solver is available under the ProLB Software License Agreement of CS Communica-
656 tion & Systemes (http://www.prolb-cfd.com/licensing-and-services/). Primary data and
657 scripts used in this study are stored in public repository (https://www.researchgate.net /
658 publication / 339901171_data_ProLB_ABL) with an individual DOI number 10.13140 /
659 RG.2.2.27679.10400. .

References

Ahmad, N. H., A. Inagaki, M. Kanda, N. Onodera, and T. Aoki (2017), Large-eddy simulation of the gust index in an urban area using the lattice boltzmann method, *Boundary-Layer Meteorology*, *163*(3), 447–467.

Andren, A., A. R. Brown, P. J. Mason, J. Graf, U. Schumann, C.-H. Moeng, and F. T. M. Nieuwstadt (1994), Large-eddy simulation of a neutrally stratified boundary layer: A comparison of four computer codes, *Quart. J. Roy. Meteor. Soc.*, *120*(520), 1457–1484, doi:10.1002/qj.49712052003.

Banerjee, T., F. De Roo, and M. Mauder (2017), Explaining the convector effect in canopy turbulence by means of large-eddy simulation, *Hydrology and Earth System Sciences*, *21*(6), 2987–3000, doi:10.5194/hess-21-2987-2017.

Bartlett, C., H. Chen, I. Staroselsky, J. Wanderer, and V. Yakhot (2013), Lattice Boltzmann two-equation model for turbulence simulations: High-Reynolds number flow past circular cylinder, *Int. J. Heat Fluid Flow*, *42*, 1–9.

Beare, R. J., and M. K. Macvean (2004), Resolution sensitivity and scaling of large-eddy simulations of the stable boundary layer, *Bound.-Layer Meteor.*, *112*(2), 257–281.

Beare, R. J., M. K. Macvean, A. A. M. Holtslag, J. Cuxart, I. Esau, J.-C. Golaz, M. A. Jimenez, M. Khairoutdinov, B. Kosovic, D. Lewellen, T. S. Lund, J. K. Lundquist, A. Mccabe, A. F. Moene, Y. Noh, S. Raasch, and P. Sullivan (2006), An intercomparison of large-eddy simulations of the stable boundary layer, *Bound.-Layer Meteor.*, *118*(2), 247–272, doi:10.1007/s10546-004-2820-6.

Blocken, B. (2015), Computational fluid dynamics for urban physics: Importance, scales, possibilities, limitations and ten tips and tricks towards accurate and reliable simulations, *Building and Environment*, *91*, 219–245.

Chateau, S., J. Favier, U. D'Ortona, and S. Poncet (2017), Transport efficiency of metachronal waves in 3d cilium arrays immersed in a two-phase flow, *Journal of Fluid Mechanics*, *824*, 931–961.

Chen, S., and G. D. Doolen (1998), Lattice Boltzmann method for fluid flows, *Annu. Rev. Fluid Mech.*, *30*(1), 329–364.

Chevillotte, F., and D. Ricot (2016), Development and Evaluation of Non-Reflective Boundary Conditions for Lattice Boltzmann Method, in *22nd AIAA/CEAS Aeroacoustics Conference*, p. 2915.

692 Cheylan, I., G. Fritz, D. Ricot, and P. Sagaut (2019), Shape optimization using the adjoint
693 lattice boltzmann method for aerodynamic applications, *AIAA Journal*, pp. 1–16.
694 Chow, F. K., R. L. Street, M. Xue, and J. H. Ferziger (2005), Explicit filtering and recon-
695 struction turbulence modeling for large-eddy simulation of neutral boundary layer flow,
696 *J. Atmos. Sci.*, *62*(7), 2058–2077.
697 Coreixas, C., G. Wissocq, G. Puigt, J.-F. Boussuge, and P. Sagaut (2017), Recursive reg-
698 ularization step for high-order lattice boltzmann methods, *Physical Review E*, *96*(3),
699 033,306.
700 Cushman-Roisin, B., and J.-M. Beckers (2009), *Introduction to geophysical fluid dynamics:*
701 *physical and numerical aspects*, Academic Press.
702 Deardorff, J. (1980), Stratocumulus-capped mixed layer derived from a three-dimensional
703 model, *Boundary-Layer Meteorology*, *18*, 495–527.
704 D'humières, D., and P. Lallemand (1986), Lattice gas automata for fluid mechanics, *Phys-*
705 *ica A: Statistical Mechanics and its Applications*, *140*(1-2), 326–335.
706 d'Humières, D., I. Ginzburg, M. Krafczyk, P. Lallemand, and L.-S. Luo (2002), Multiple-
707 relaxation-time lattice Boltzmann models in three dimensions, *Phil Trans R Soc Lond A*,
708 *360*, 437–451.
709 Dipankar, A., B. Stevens, R. Heinze, C. Moseley, G. ZÃďngl, M. Giorgetta, and S. Brdar
710 (2015), Large eddy simulation using the general circulation model icon, *Journal of Ad-*
711 *vances in Modeling Earth Systems*, *7*(3), 963–986, doi:10.1002/2015MS000431.
712 Dyer, A. J. (1974), A review of flux-profile relationships, *Bound.-Layer Meteor.*, *7*(3),
713 363–372, doi:10.1007/BF00240838.
714 Eggels, J. G. (1996), Direct and large-eddy simulation of turbulent fluid flow us-
715 ing the lattice-Boltzmann scheme, *Int. J. Heat Fluid Flow*, *17*(3), 307 – 323, doi:
716 http://dx.doi.org/10.1016/0142-727X(96)00044-6.
717 Feng, Y., P. Boivin, J. Jacob, and P. Sagaut (2019a), Hybrid recursive regularized lattice
718 boltzmann simulation of humid air with application to meteorological flows, *Physical*
719 *Review E*, *100*(2), 023,304.
720 Feng, Y., S. Guo, J. Jacob, and P. Sagaut (2019b), Solid wall and open boundary condi-
721 tions in hybrid recursive regularized lattice boltzmann method for compressible flows,
722 *Physics of Fluids*, *31*, 126,103.
723 Fernando, H., S. Lee, J. Anderson, M. Princevac, E. Pardyjak, and S. Grossman-Clarke
724 (2001), Urban fluid mechanics: air circulation and contaminant dispersion in cities, *En-*

vironmental Fluid Mechanics, *1*(1), 107–164.

Gao, T., Y.-H. Tseng, and X.-Y. Lu (2007), An improved hybrid cartesian/immersed boundary method for fluid–solid flows, *International Journal for Numerical Methods in Fluids*, *55*(12), 1189–1211.

Grabowski, W. W., and P. K. Smolarkiewicz (1990), Monotone finite-difference approximations to the advection-condensation problem, *Mon. Wea. Rev.*, *118*, 2082–2097.

Heerwaarden, C. C. v., B. J. Van Stratum, T. Heus, J. A. Gibbs, E. Fedorovich, and J. P. Mellado (2017), Microhh 1.0: a computational fluid dynamics code for direct numerical simulation and large-eddy simulation of atmospheric boundary layer flows, *Geoscientific Model Development*, *10*(8), 3145–3165.

Hirsch, C. (2007), *Numerical computation of internal and external flows: The fundamentals of computational fluid dynamics*, Elsevier.

Hou, S., J. Sterling, S. Chen, and G. Doolen (1994), A lattice Boltzmann subgrid model for high Reynolds number flows, *arXiv preprint comp-gas/9401004*.

Jacob, J., and P. Sagaut (2018), Wind comfort assessment by means of large eddy simulation with lattice boltzmann method in full scale city area, *Building and Environment*, *139*, 110–124.

Jacob, J., O. Malaspinas, and P. Sagaut (2018), A new hybrid recursive regularised bhatnagar–gross–krook collision model for lattice boltzmann method-based large eddy simulation, *Journal of Turbulence*, *19*(11-12), 1051–1076.

Kim, K. H., C. Kim, and O.-H. Rho (2001), Methods for the accurate computations of hypersonic flows: I. AUSMPW+ scheme, *Journal of Computational Physics*, *174*(1), 38–80.

Latt, J., and B. Chopard (2006), Lattice Boltzmann method with regularized pre-collision distribution functions, *Mathematics and Computers in Simulation*, *72*, 165–168.

Malaspinas, O. (2015), Increasing stability and accuracy of the lattice Boltzmann scheme: recursivity and regularization, *ArXiv e-prints*.

Malaspinas, O., and P. Sagaut (2012), Consistent subgrid scale modelling for lattice-boltzmann methods, *Jurnal of Fluid Mechanics*, *700*, 514–542.

Markkanen, T., Ü. Rannik, B. Marcolla, A. Cescatti, and T. Vesala (2003), Footprints and fetches for fluxes over forest canopies with varying structure and density, *Boundary-Layer Meteorology*, *106*(3), 437–459, doi:10.1023/A:1021261606719.

Maronga, B., M. Gryschka, R. Heinze, F. Hoffmann, F. Kanani-Sühring, M. Keck, K. Ketelsen, M. O. Letzel, M. Sühring, and S. Raasch (2015), The parallelized large-eddy simulation model (palm) version 4.0 for atmospheric and oceanic flows: model formulation, recent developments, and future perspectives, *Geoscientific Model Development Discussions 8 (2015), Nr. 2, S. 1539-1637*.

Mattila, K. K., P. C. Philippi, and L. A. HegeleJr. (2017), High-order regularization in lattice-Boltzmann equations, *Physics of Fluids*, *29*(4), 046,103, doi:10.1063/1.4981227.

Merlier, L., J. Jacob, and P. Sagaut (2019), Lattice-boltzmann large-eddy simulation of pollutant dispersion in complex urban environment with dens gas effects: Model evaluation and flow analysis, *Building and Environment*, *148*, 634–652.

Moeng, C. (1984), A large-eddy-simulation model for the study of planetary boundary-layer turbulence, *Journal of Atmospheric Sciences*, *41*, 2052–2062.

Nebenführ, B., and L. Davidson (2015), Large-eddy simulation study of thermally stratified canopy flow, *Boundary-Layer Meteorology*, *156*(2), 253–276, doi:10.1007/s10546-015-0025-9.

Nieuwstadt, F. T., P. J. Mason, C.-H. Moeng, and U. Schumann (1993), Large-eddy simulation of the convective boundary layer: A comparison of four computer codes, in *Turbulent shear flows 8*, pp. 343–367, Springer.

Premnath, K. N., M. J. Pattison, and S. Banerjee (2009a), Dynamic subgrid scale modeling of turbulent flows using lattice-Boltzmann method, *Physica A: Statistical Mechanics and its Applications*, *388*(13), 2640 – 2658, doi: http://dx.doi.org/10.1016/j.physa.2009.02.041.

Premnath, K. N., M. J. Pattison, and S. Banerjee (2009b), Generalized lattice Boltzmann equation with forcing term for computation of wall-bounded turbulent flows, *Phys. Rev. E*, *79*, 026,703, doi:10.1103/PhysRevE.79.026703.

Pressel, K. G., C. M. Kaul, T. Schneider, Z. Tan, and S. Mishra (2015), Large-eddy simulation in an anelastic framework with closed water and entropy balances, *Journal of Advances in Modeling Earth Systems*, *7*(3), 1425–1456.

Prusa, J. M., P. K. Smolarkiewicz, and A. A. Wyszogrodzki (2008), Eulag, a computational model for multiscale flows, *Computers & Fluids*, *37*(9), 1193–1207.

Qian, Y., D. d'Humières, and P. Lallemand (1992), Lattice BGK models for Navier-Stokes equation, *Europhysics Letters*, *17*(6), 479–484.

Robins, A., P. Hayden, and E. M. M. Wingstedt (2016), MODITIC wind tunnel experiments, *Tech. Rep. FFI-RAPPORT 16/01483*, Norwegian Defence Research Establishment.

Sagaut, P. (2006), *Large eddy simulation for incompressible flows: an introduction*, Springer Science & Business Media.

Sagaut, P. (2010), Toward advanced subgrid models for lattice-boltzmann-based large-eddy simulation: Theoretical formulations, *Computers and Mathematics with Applications*, *59*, 2194–2199.

Schmidt, H., and U. Schumann (1989), Coherent structure of the convective boundary layer derived from large-eddy simulations, *J. Fluid Mech.*, *200*, 511–562.

Senocak, I., A. S. Ackerman, M. P. Kirkpatrick, D. E. Stevens, and N. N. Mansour (2007), Study of near-surface models for large-eddy simulations of a neutrally stratified atmospheric boundary layer, *Bound.-Layer Meteor.*, *124*(3), 405–424, doi:10.1007/s10546-007-9181-x.

Shepard, D. (1968), A two-dimensional interpolation function for irregularly-spaced data, in *Proceedings of the 1968 23rd ACM national conference*, pp. 517–524, ACM.

Siebesma, A., and J. Cuijpers (1995), Evaluation of parametric assumptions for shallow cumulus convection, *Journal of the atmospheric sciences*, *52*(6), 650–666.

Siebesma, A. P., C. S. Bretherton, A. Brown, A. Chlond, J. Cuxart, P. G. Duynkerke, H. Jiang, M. Khairoutdinov, D. Lewellen, C.-H. Moeng, E. Sanchez, B. Stevens, and D. E. Stevens (2003), A large eddy simulation intercomparison study of shallow cumulus convection, *J. Atmos. Sci.*, *60*(10), 1201–1219, doi:10.1175/1520-0469(2003)60<1201:ALESIS>2.0.CO;2.

Sommeria, G. (1976), Three-dimensional simulation of turbulent processes in an undisturbed trade wind boundary layer, *J. Atmos. Sci.*, *33*, 216–241.

Stevens, B., C.-H. Moeng, A. S. Ackerman, C. S. Bretherton, A. Chlond, S. de Roode, J. Edwards, J.-C. Golaz, H. Jiang, M. Khairoutdinov, et al. (2005), Evaluation of large-eddy simulations via observations of nocturnal marine stratocumulus, *Monthly weather review*, *133*(6), 1443–1462.

Teixeira, C. M. (1998), Incorporating turbulence models into the lattice-Boltzmann method, *International Journal of Modern Physics C*, *9*(08), 1159–1175.

Wilhelm, S., J. Jacob, and P. Sagaut (2018), An explicit power-law-based wall model for lattice-Boltzmann-method-Reynolds-averaged numerical simulations of the flow around

822 airfoils, *Physics of Fluids*, *30*, 065,111.

823 Xu, H., and P. Sagaut (2013), Analysis of the absorbing layers for the weakly-compressible
824 lattice Boltzmann methods, *J. Comput. Phys.*, *245*, 14–42.

825 Yu, H., L.-S. Luo, and S. S. Girimaji (2006), LES of turbulent square jet flow using an
826 MRT lattice Boltzmann model, *Computers & Fluids*, *35*(8), 957–965.

827 Zhang, R., H. Fan, and H. Chen (2011), A lattice Boltzmann approach for solving scalar
828 transport equations, *Philosophical Transactions of the Royal Society of London A: Mathe-*
829 *matical, Physical and Engineering Sciences*, *369*(1944), 2264–2273.